electronics

MDPI

Article

Study of Algorithms for Wind Direction Retrieval from X-Band Marine Radar Images

Hui Wang [1], Haiyang Qiu [1,*], Pengfei Zhi [1], Lei Wang [2], Wei Chen [1], Rizwan Akhtar [1] and Muhammad Asif Zahoor Raja [3]

1 School of Electronics and Information, Jiangsu University of Science and Technology, Zhenjiang 212003, China
2 State Key Laboratory of Information Engineering in Surveying, Mapping and Remote Sensing, Wuhan University, Wuhan 430079, China
3 Department of Electrical and Computer Engineering, COMSATS University Islamabad, 43600 Attock Campus, Pakistan
* Correspondence: hy.qiu@just.edu.cn; Tel.: +86-1889-665-8699

Received: 29 April 2019; Accepted: 5 July 2019; Published: 8 July 2019

Abstract: After decades of research, X-band marine radars have been broadly used for wind measurement. For retrieving the wind direction based on the wind-induced streaks, a lot of effort has been expended on three celebrated approaches—the local gradient method (LGM), the adaptive reduced method (ARM), and the energy spectrum method (ESM). This paper presents a scientific study of these methods. The contrast of retrieving the real measured marine radar images and vane measured results is evaluated, in perspective of the error statistics and algorithm operation efficiency. Interference factors, such as the historical information of the measured area, reference wind speed, and sea condition showing in the monitoring equipment are also concerned. The tentative results showed that LGM is robust, which can be implemented in most radar images, because it allows for a lower selection of requirements compared with the other two methods. For ARM, the better retrieval performance is a tradeoff with extra computation, which is expensive. ESM is superior to the other two algorithms in terms of accuracy and computation load; however, this algorithm is sensitive in rain-contaminated radar images, meaning it is a good choice for data post-processing in the lab.

Keywords: marine radar; wind direction retrieval; small wind streak; local gradient method; adaptive reduced method; energy spectrum method

1. Introduction

A near-surface wind field is formed by the horizontal movement of air relative to the sea surface, which is an important driving force for marine dynamics. Wind field parameters are imperative for the safety of navigation and marine engineering, necessary for military activities such as vessels' or ships' voyages. Conventional wind direction measurement methods are classified into two categories—site-based measurement and remote sensing. Site-based measurement can obtain ocean wind direction information through a wind vane [1], however this method may be influenced by the surrounding environment, such as platform movement or vile weather. Additionally, it is difficult to mount a vane in a remote ocean area, and to have a wind field error of up to 10% [2]. At present, remote sensing mainly depends on spaceborne/airborne microwave scatterometers [3], SARs [4], and so on. These devices can capture a large area of ocean wind field information, however, as they are restricted to a low spatial resolution, it is difficult for them to consistently monitor sea surface wind, and they are vulnerable to weather or other defects at the same time [5].

In order to make up for the deficiency existing in remote sensing measurement, low-cost marine X-band radars, with the advantage of high resolution and timely feedback, have been broadly used in many monitoring scenarios. X-band radar image sequences have previously been used to measure two-dimensional wave spectra in order to retrieve sea wave components [6,7]. The image sequences of the ocean surface can be utilized for target identification [8], detection [9], mean near-surface current measurement [10], and current field measurement [11]. Specially, X-band radar image sequence is becoming the state-of-the-art for wind field retrieving [12].

By operating at a low grazing angle, the transmitting signal can be reflected by the sea surface to form backscatter, which is mainly caused by sea surface roughness. Both a long surface gravity and local wind can modulate the roughness, thus generating radar images [13]. Particularly, small-scale roughness is highly dependent on local wind; hence, the wind direction can be retrieved accordingly, based on collecting marine radar images.

From a graphic perspective, the normalized radar cross section (NRCS), indicating an intensity level of radar echo, keeps a high correlation with the wind speed and direction. NRCS has only one peak in the upwind direction, and a minimum in the crosswind direction—simultaneously, it is an exponential function of wind speed [14]. According to these characters, two key approaches are posed for wind direction retrieval from X -band radar image sequences [15].

The first one is based on the relationship of NRCS and the radar look direction—this approach necessitates the azimuth being equal or greater than 180°, which is difficult to realize for shore-based radars because of the sheltering of land [16]. Recently, Lund et al. [17] and Vicen Bueno et al. [18] utilized the same principle to retrieve wind field information with independent platform movement. However, the abovementioned two methods neglect the following crucial factors: in cases of low sea states' circumstances—the obstruction of the radar field and the appearance of islands—the wind measurement errors will be increased [19]. Although the latter method has been improved by Ying Liu et al. [19], it cannot be applied to local X-band radar images or to a sheltering of land greater than 180° [20].

The second approach is based on small-scale streaks modulated by the wind in radar images—the determined wind directions as the orientations of the wind streaks that are approximately aligned with the mean surface wind direction. A large amount of literature has proven that this method has the advantage of high precision, fast operation, and is robust in a variety of circumstances, and it has thus gradually dominated X-band sea environmental monitoring [21–23]. There are quite a few algorithms for small-scale streak retrieving, including, but not limit to, the local gradient method (LGM), the adaptive reduced method (ARM), the energy spectrum method (ESM), and the optical flow-based motion (OFM). Because a wind field is in the presence of static signals as a result of the radar image sequence, the outcome of the OFM algorithm has a lower accuracy that will not meet the demand of an actual sea monitoring project [24]; thus, we dropped this approach for this paper. LGM needs to iteratively smooth and subsample the wind streaks' images three times in order to obtain a so-called Gaussian pyramid. From each of these images, the local wind directions are computed using the standard local gradient [25]. ARM puts forward an adaptive reduction operator, which means that the algorithm can automatically select the reduction operator with a different step size according to the judgment result, and the local wind directions are computed using the adaptive local gradient [26]. ESM is proposed for extracting the wind direction through wind streaks' image energy spectrum—the wind direction gained directly from the energy spectrum image based on the energy concentrated areas perpendicular to the wind streaks [27]. To the authors' knowledge, there is limited literature making an explicit comparison of the three algorithms using real-time collected radar data. The main contribution of this paper lies in that we, in detail, analyze and compare the three algorithms' performance error statistics and operating efficiency, and simultaneously consider the influence factors, which are helpful and vital for engineering realization problems.

The data for analyzing and researching is gathered by the HEU wave monitoring system, which is developed by the HEU marine monitoring research group [28,29]. The remainder of the paper is organized as follows. Section 2 presents a preliminary introduction of wind feature extraction from a small-scale wind streak. In Section 3, we give a review and contrast of LGM, ARM, and ESM. These methods are analyzed and discussed with the testing data in Section 4. Finally, we draw a conclusion in Section 5.

2. Data and System Model Overview

The above-mentioned algorithms cannot be directly used for the collection of raw radar data, as the mapped objective is a small-scale wind streak. This section will give an overview of the data collection, and will introduce the data pre-processing in terms of rain recognition and image filtering, in order to extract small-scale wind streaks initially.

2.1. Data Overview

The data used for testing was collected from the Pingtan General Testing Ground, an institution in the south of Haitan Island, the Fujian Province of China. Haitan Island is the fifth largest Chinese sea island, located between the Taiwan Strait and Haitan Strait. The average depth of the radar-measured sea area is about 28 m; this area often happens in high-sea conditions due to terrain and strong storms. The measured tidal level difference is up to 5 m, accompanied by an average wind speed of about 6.9 m/s. The average strong-wind (over seven level) days are nearly 125 days a year. Strong storms happen about 6.3 times a year, which indicates that the ground is one of the strongest wind areas in Fujian Province. The test site can provide abundant data for algorithm analyzing. Figure 1 shows how the HEU wave monitoring system collects and records data at this site, in which a standard RM-1290 marine X-band radar is mounted on top of a platform tower.

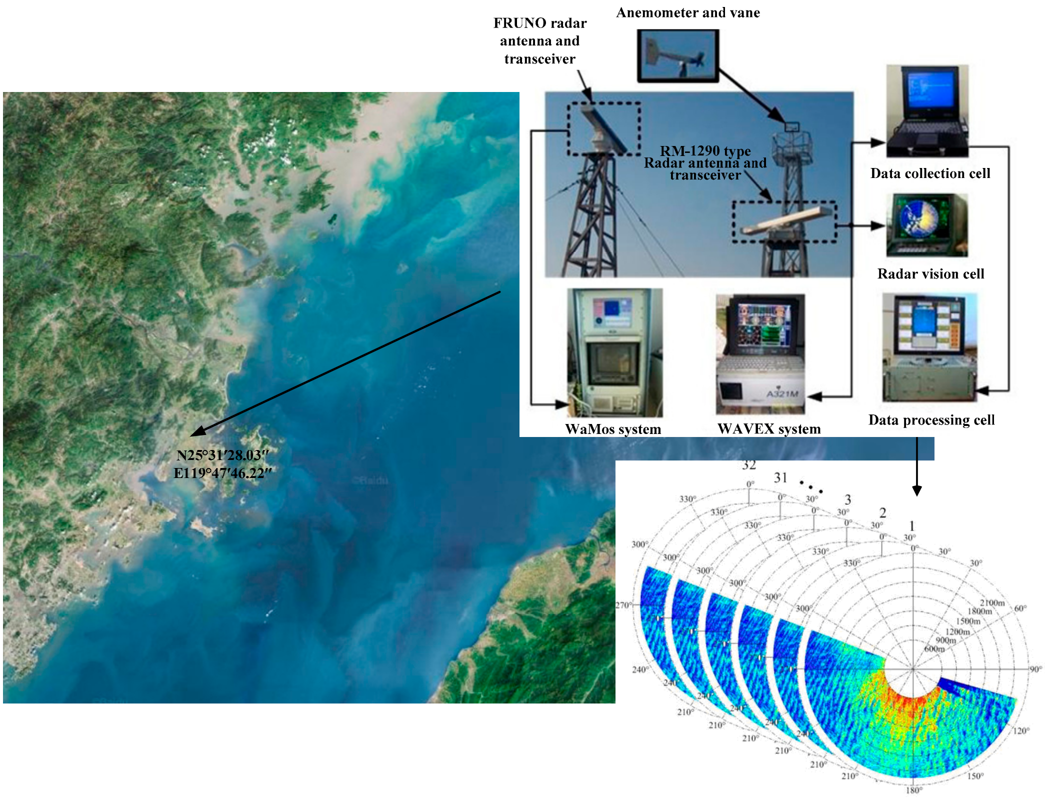

Figure 1. The testing site as well as the monitoring equipment.

The radar transceiver signal is replicated into triplet form—the replicated signal is sent to the data acquisition unit, radar display unit, and data processing unit, respectively. For reference, another piece of sophisticated equipment, WAVEX, works simultaneously, so as to measure the wave height and sea current direction. The X-band marine radar operates at a low grazing incidence with horizontal polarization in the transmitting and receiving process—it belongs to a sort of shot pulsed radar with a pulse width of 0.5–10 µs. The radar operates at 9.4 GHZ, with a sampling frequency of 20 MHz The specifications detail of the RM-1290 marine radar are shown in Table 1.

Table 1. Specifications of the RM-1290 marine radar. HH—horizontally; RF—radiofrequency; IF—infrared.

Antenna Rotating Speed	26^{+2}_{-6} **rpm**
Gain	28.5 dB
Polarization	HH
Horizontal beam width	≤1.3° (antenna of 1.8 m)
Vertical beam width	23° ± 2
Radio frequency	9410 ± 30 MHz
RF pulse envelope width	Short pulse: $0.05^{+0.03}_{-0.02}$ μs
Pulse repetition frequency	Short pulse: 1300 (± 10%) Hz
RF pulse peak power	Short pulse: ≥16 KW
Receiver IF bandwidth	Short pulse: 20 ± 3 MHz
Distance resolution	≤23 m
Azimuth resolution	≤1.3°

The radar antenna rotatory period is 2.5 s (24 rpm), with a pulse repetition frequency of 1.3 kHz. Each of the radar-image sequences collected here consists of 32 images, with a time interval of 80 s. Using the azimuth-range bin and scales data, the monitoring system digitizes the radar backscatter intensity into a 14-bit, that is, digitized back-scatter intensity, in the range of 0 to 8192 ($2^{(14\text{-}1)}$), as shown at the right bottom corner in Figure 1.

2.2. *Data Pre-Processing*

Before using the radar data to retrieve the wind direction, a basic data pre-processing quality control procedure should be conducted. The procedure includes the rain recognition and image filter.

2.2.1. Rain Recognition

All of the methods work only for rain-free radar images, which have to been automatically selected depending on the rain recognition data pre-processing. Lund et al. [17] proposed using the zero-pixel percentage (ZPP) in the whole radar image in order to identify the rainfall radar image. Considering the influence of sea conditions on the statistical results, this paper will extend a method for rainfall image recognition based on the statistical results of ZPP in the occlusion area of a radar image. The ZPP is as follows:

$$P = \frac{f_0}{f} \tag{1}$$

where f is the total number of pixels in the radar image, and f_0 is the number of normalized zero intensity pixels.

No matter whether using a ship-based or shore-based navigation radar image, when the propagation route of the radar electromagnetic wave is blocked because of obstacles such as a chimney, mast, island, and so on, a large number of invalid signals will be generated in the radar image, resulting in a fanned shadow area (shielding area) in the radar image. When there is no rain, the shielding area is almost blue, and there is no radar echo. When there is rainfall, the raindrop can reflect the radar electromagnetic wave signal and generate uniform backscattering, so that the blocking area appears as flaky rain echo. As the zero-intensity percentage of the statistical occlusion area will not be affected by the change of sea conditions, it will be more effective and accurate to detect whether the radar image is affected by rainfall.

Figure 2 shows the occlusion zero pixel proportion (OZPP) distribution of 200 radar images, in which the selected radar region is 80–600 points in the radial direction, and 50–90 degrees in the azimuth direction. The rectangular area in the figure is the data of the rainfall in the radar image. As can be seen from the figure, when there is no rain, the OZPP basically maintains a stable change range, very close to 1, because there is almost no radar echo at this time. When rainfall occurs, the percentage of zero-intensity in the shielding area decreases immediately by a large margin. Finally, according to the statistical results, 0.94 is selected as the threshold to detect whether the radar image is affected by rainfall. When the OZPP is greater than 0.94, it indicates that there is no rainfall in the detection area; when the OZPP is less than 0.94, it can be determined that there is rainfall in the detection area.

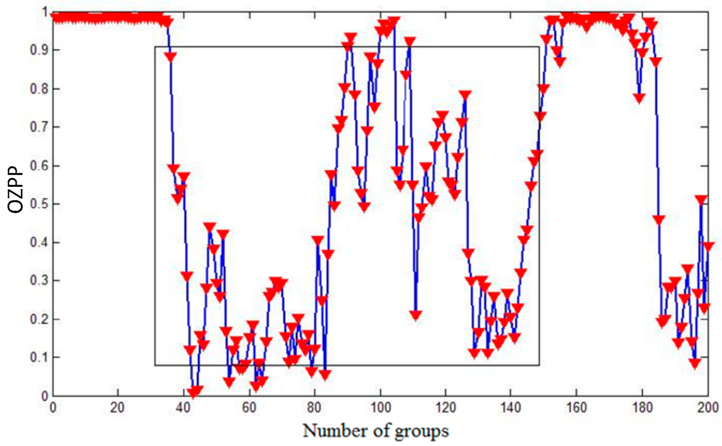

Figure 2. The OZPP distribution of 200 radar images.

2.2.2. Image Filter

In order to effectively remove the influence of the same frequency, a small amount of rainfall, and a small target on the radar image, it is necessary to filter the radar images to the extract the sea wind direction. While a linear filter will alter the intrinsic features of the radar images, a nonlinear median filter, which not only owns a superior denoising performance, but also has a protective effect on the image detail features, is more preferable in this paper. Median filtering is implemented by overlapping the slide window with the image; the gray value of the pixel in the window is arranged according to a monotonic rise or monotonic fall. A median filtered image is obtained by traversing the slide window over the entire image. It can be written as follows:

$$g(x, y) = median\{f(x - i, y - j), (i, j) \in W\} \quad (2)$$

where $g(x, y)$ represents the filtered image, $f(x - i, y - j)$ is the input image, and W represents the slide window. According to the resolution of the input data, the size of W is determined to be 3×3.

2.3. Small Scale Wind Streak Characteristics Extraction

Some streaks can form, evolve, and decay over relatively short lifetimes of only dozens of minutes, and then rapidly regenerate—so, it is named "small-scale wind streak" [30,31]. The light and dark stripes' characteristics modulated by wind fields exist in marine radar images. The experimental results show that the change of roughness caused by the turbulence of wind shear stress can be detected by marine radar, and these results can be reflected on the radar image in a stripe distribution [32]. The relationship between the near-surface wind vector and NRCS can be described by a geophysical model function (GMF), as described in [14]:

$$\sigma^0 = A(\theta)u^{\gamma(\theta)}(1 + B(u, \theta)\cos\Phi + C(u, \theta)\cos 2\Phi) \quad (3)$$

where σ^0 and u represent the NRCS and wind speed, respectively; Φ means the angle between the radar look and wind direction; and θ is the angle of grazing incidence. A, B, C, and γ, typically determined by the radar frequency and polarization mode, are empirical parameters. It is well known that NRCS represents the level of near-surface roughness, and the GMF model shows that there is a high correlation with the wind field. Thus, wind streaks possessing same distribution characteristics with near-surface roughness will exist in the X-band marine radar image. In other words, the wind streaks characteristics are consistent with the stripe-like turbulence characteristics, and exist in the marine radar image sequence, shown as light-, dark-, and small-scale forms. The visible streaks in the radar images hover around 200 m to 500 m; these streaks have been shown to be well aligned with the mean surface wind direction, with their frequency being close to static.

The small-scale wind streaks cannot be observed in a single radar image, because of the single observation lasting for only a few seconds, whereas the small-scale wind streaks have static features. The following formulation shows how to separate wind from other signatures according to the small-scale wind streak evolving period. Firstly, integrate a set of radar-image sequences (typically, 32 images representing 80 s duration of data) over time, and then construct an image space low-pass filter to average the radar image at the same position's pixel points, as follows [33]:

$$f(\theta, r) = \frac{\sum\limits_{t=0}^{N_t} f(\theta, r, t)}{N_t} \tag{4}$$

where $f(\theta, r)$ represents the sea surface static feature image, including the numbers of the small scale wind streaks, which we are interested in; $f(\theta, r, t)$ is the single radar image at time t; θ and r are the radar image azimuth angle and radial radius; and N_t is the sum of the sequence. In the following, we will compare three kinds of sea surface wind retrieval algorithms based on $f(\theta, r)$.

3. Review and Illustration of LGM, ARM, and ESM

In this section, we firstly give a review of three different wind-direction retrieval methods of the ocean surface based on small-scale wind streaks, and then a complexity comparison of the three algorithms is discussed.

3.1. The Traditional LGM

Under the assumption that small-scale streaks are supposed to be approximately parallel with the mean wind direction, LGM can retrieve the wind direction by using a space domain iterative to reduce and smooth; the flow chart of LGM is shown in Figure 3.

The reduce process in Step 4 can be computed, depending on the Gaussian pyramid (GP), as follows:

$$F_{G1} = C_{(\downarrow 2)} F \tag{5}$$

$$C_{(\downarrow 2)} = \frac{1}{4}\begin{bmatrix} 1 & 1 \\ 1 & 1 \end{bmatrix} \tag{6}$$

where $C_{(\downarrow 2)}$ is the GP reduce operator, and the subscript means that the sampling rate is 2. F denotes the original image, and F_{G1} is the first-time reduced image. F_{G1} needs to be smoothed in order to filter out the high-frequency signals, this process uses both fourth- and second-order Yang hui triangular filter matrixes, as follows:

$$H^4 = \frac{1}{256}\begin{bmatrix} 1 & 4 & 6 & 4 & 1 \\ 4 & 16 & 24 & 16 & 4 \\ 6 & 24 & 36 & 24 & 6 \\ 4 & 16 & 24 & 16 & 4 \\ 1 & 4 & 16 & 4 & 1 \end{bmatrix} H^2 = \frac{1}{16}\begin{bmatrix} 1 & 2 & 1 \\ 2 & 4 & 2 \\ 1 & 2 & 1 \end{bmatrix} \tag{7}$$

to formulate an operator for $R = H^2 C_{(\downarrow_K)} H^4$, the image including the wind streaks (sea surface static feature image) has firstly been denoted to be as follows: $F_{R1} = RF_{G1}$; the smooth process does not change the image resolution. For an equivalent of the wind steak scale, the upper entire process, including reducing and smoothing, has to repeated three times, and finally, we obtain F_{R3}.

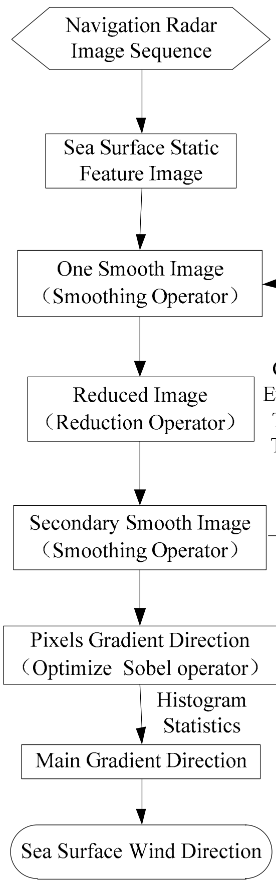

Figure 3. The flow chart of the local gradient method (LGM).

With F_{R3}, the gradient direction of the wind streaks image can be calculated by applying the optimized Sobel operator along the x and y axes. Then, we have $W_X = D_x F_{R3}$ and $W_Y = D_Y F_{R3}$, and the optimized Sobel operator is as follows:

$$\begin{cases} D_x = \frac{1}{32}\begin{bmatrix} 3 & 0 & -3 \\ 10 & 0 & -10 \\ 3 & 0 & -3 \end{bmatrix} \\ D_y = {D_x}^T \end{cases} \tag{8}$$

Hence, the main sea wind direction can be obtained by the normal main gradient direction. Danker [21] has verified the effectiveness of this method, but he did not consider whether the subsampled image resolution could march with the streaks scale or not. This may lead to a lower accuracy, with some data being unavailable.

3.2. The Improved ARM

On the basis of the LGM algorithm, ARM uses an adaptive reduction operator, and this means that ARM can automatically select the reduction operator based on the loop index of K, and then determine the dimension size of the slide window. The flow chart of ARM is shown in Figure 4. The adaptive reduction operator is shown, as follows:

$$C_{\downarrow K} = \frac{1}{K}\left[\left.\begin{bmatrix} 1 \\ 1 \\ \vdots \\ 1 \end{bmatrix}\right\}\mathrm{K}\right] \times \frac{1}{K}\underbrace{\begin{bmatrix} 1 & 1 & \cdots & 1 \end{bmatrix}}_{\mathrm{K}} = \frac{1}{K^2}\left[\left.\underbrace{\begin{bmatrix} 1 & 1 & \cdots & 1 \\ 1 & 1 & \cdots & 1 \\ 1 & 1 & \ddots & \vdots \\ 1 & 1 & \cdots & 1 \end{bmatrix}}_{\mathrm{K}}\right\}\mathrm{K}\right] \tag{9}$$

where $C_{(\downarrow K)}$ is the reduction operator of the reduced rate K; according to the marine radar resolution, the rate can be determined as K= 2, 3, ... 8, in which scope maximum value is 8. The flow chart of ARM is shown in Figure 4. The reduce process using $C_{(\downarrow K)}$ can be similarly computed, depending on the Gaussian pyramid (GP), as follows:

$$F_{GK} = C_{(\downarrow K)}F \tag{10}$$

The image uses H^4 to smooth before and after the reduction so as to filter out the high frequency noise, and then formulate an operator for $R = H^2C_{(\downarrow K)}H^4$; the image including the wind streaks has been denoted to be $F_{RK} = RF_{GK}$, and the smoothing process does not change the resolution of the image. For a match of the wind steak scale, the upper entire process, including the reducing and smoothing, has to repeat N times, and then we obtain F_{RK}. The gradient of each pixel along the x and y axes can be written as follows:

$$\begin{cases} W_x = F_{RK} * \mathrm{D_x} \\ W_y = F_{RK} * \mathrm{D}_y \end{cases} \tag{11}$$

Thus, the gradient direction W_θ of each pixel is obtained, as follows:

$$W_\theta = \arctan\frac{W_y}{W_x} \tag{12}$$

Histogram statistics were performed for all of the pixel gradient directions. From the probability distribution map of the gradient direction, we could get the direction with the maximum frequency $W_{\theta_{\max}}$. In order to calculate the stability factor, we selected all of the gradient directions in the range of $\lambda W_{\theta_{\max}} \sim W_{\theta_{\max}}$, where λ is a scale parameter, and can be chosen depending on the practical situation. In this paper, we choose $\lambda = 0.7$, and the array of direction consisted of $W_P = \left[W_1, W_2, \cdots W_p\right]$.

ARM uses an optimal reduction rate and stability coefficient to determine when the image reduction process should stop. It is upon this that the reduced image resolution and scale of the small-scale wind streaks can achieve the best ratio. The stability coefficient (η) can be calculated, as follows:

$$\eta = \frac{\sqrt{\frac{1}{p-1}\sum_{i=1}^{p}\left(W_i - \frac{1}{p}\sum_{i=1}^{p} W_i\right)^2}}{\frac{1}{p}\sum_{i=1}^{p} W_i} \times 100\% \tag{13}$$

where, W_i is i-th pixel gradient value of the reduced image, $i = 1,\ 2,\ 3, \cdots p$ and p is the amount of pixels. The stability coefficient (η) means the aggregation density of the gradient direction W_i; if η is small, the distribution of gradient direction is dense, and vice versa. A dense gradient direction can better reflect the wind streak information, while a sparse one indicates an implicit interference of another signal. Figure 5 shows the reduction rate for the $K = 2$ and $K = 7$ gradient direction probability distribution on a set of collected radar data. The maximum probability of the gradient direction is 0.012 when the reduction rate is $K = 2$. The maximum probability of the gradient direction is 0.025 when the reduction rate is $K = 7$. So, $K = 7$ is the optimal reduction rate in ARM. At the optimal reduction rate, the reduced image resolution more closely matches the small-scale wind streak. From the data, it is shown that the ARM result for the wind direction is about 37°, and the anemometer result for the wind direction about 35°.

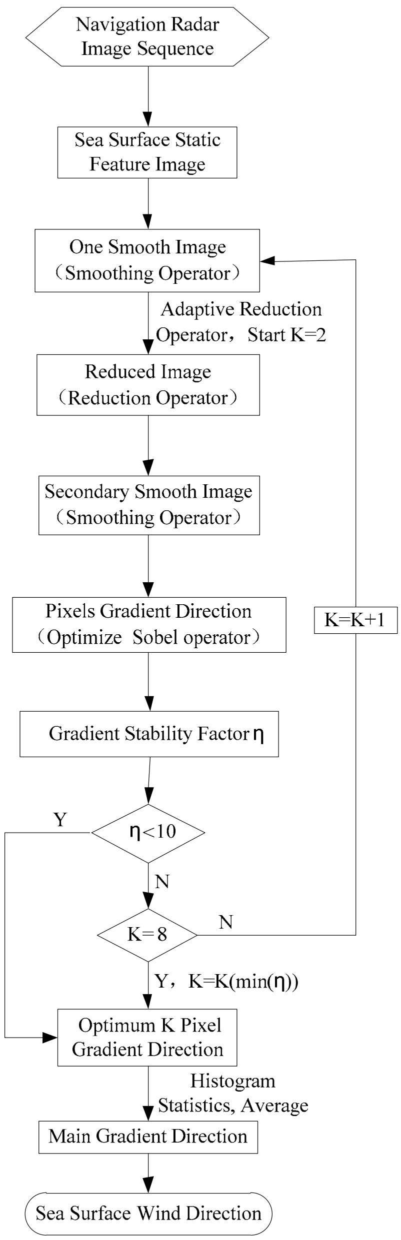

Figure 4. The flow chart of the adaptive reduced method (ARM).

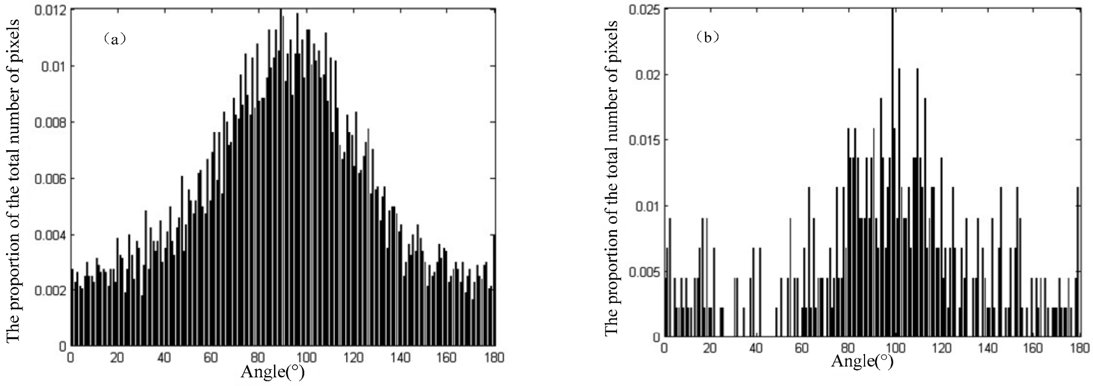

Figure 5. (**a**) $K = 2$: gradient direction probability distribution. (**b**) $K = 7$: gradient direction probability distribution.

3.3. The New ESM

Unlike retrieving the wind direction in the spatial domain, the ESM algorithm is posed in order to extract the wind direction through the SAR image energy spectrum. The flow chart of the ESM is shown in Figure 6.

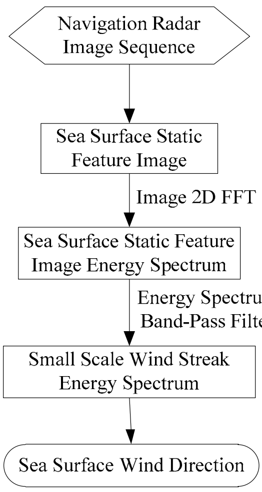

Figure 6. The flow chart of the energy spectrum method (ESM).

The two-dimensional image is composed of sins and cosines signals with different frequencies, amplitudes, and phases. Thus, the energy spectrum distribution of the 2D image can be obtained by 2D FFT. The mathematical model of the 2D FFT for the two-dimensional sea surface static feature images, $g(x, y)$, in Cartesian coordinates, is as follows:

$$F(k_x, k_y) = \sum_{i=1}^{N_x} \sum_{j=1}^{N_y} g(x_i, y_j) \exp[-i * 2\pi(\frac{x_i * k_x}{\max(x_i)} + \frac{y_j * k_y}{\max(y_j)})] \tag{14}$$

where, $F(k_x, k_y)$ is the Fourier coefficient of $g(x, y)$, (k_x, k_y) is the frequency domain coordinates, and N_x and N_y are the pixel elements of $g(x, y)$ in the space domain, respectively. In the formula, the complex exponential term can be expanded as follows:

$$\exp[-i * 2\pi(\frac{x_i * k_x}{\max(x_i)} + \frac{y_j * k_y}{\max(y_j)})] = \cos 2\pi(\frac{x_i * k_x}{\max(x_i)} + \frac{y_j * k_y}{\max(y_j)}) + i \sin 2\pi(\frac{x_i * k_x}{\max(x_i)} + \frac{y_j * k_y}{\max(y_j)}) \tag{15}$$

with the relationship of the wavenumber and wavelength ($k_x = \frac{2\pi}{\max(x_i)*d_x}$ and $k_y = \frac{2\pi}{\max(y_j)*d_y}$, respectively), d_x and d_y are the radial and amplitude resolution of the radar image, respectively. As $F(k_x, k_y)$ has both an imaginary and real part, using Equation (14), we can obtain the energy spectrum $A(k_x, k_y)$ of the static characteristic image, $g(x, y)$, as follows:

$$A(k_x, k_y) = \sqrt{\left[\mathrm{Re}(F(k_x, k_y))\right]^2 + \left[\mathrm{Im}(F(k_x, k_y))\right]^2} \tag{16}$$

where $\mathrm{Re}(F(k_x, k_y))$ is the real part of $F(k_x, k_y)$, and $\mathrm{Im}(F(k_x, k_y))$ is the imaginary part of $F(k_x, k_y)$. ESM uses a small-scale wind streak band-pass filter to extract the small-scale streak energy spectrum. This band-pass filter can be shown as follows:

$$I(k_x, k_y) = \begin{cases} A(k_x, k_y)(\sqrt{{k_x}^2 + {k_y}^2} \in [|k_d|, |k_t|]), \\ 0(\text{else}) \end{cases} \tag{17}$$

where $I(k_x, k_y)$ is the energy spectrum of the wind streaks, and $k_d = \frac{2\pi}{L_t}$ is the wind streak energy spectrum wave number low-limit, where L_t is the scale upper-limit. Similarly, $k_t = \frac{2\pi}{L_d}$ is the upper-limit, where L_d is the scale low-limit. The small-scale wind streaks wave number energy spectrum is shown in Figure 7.

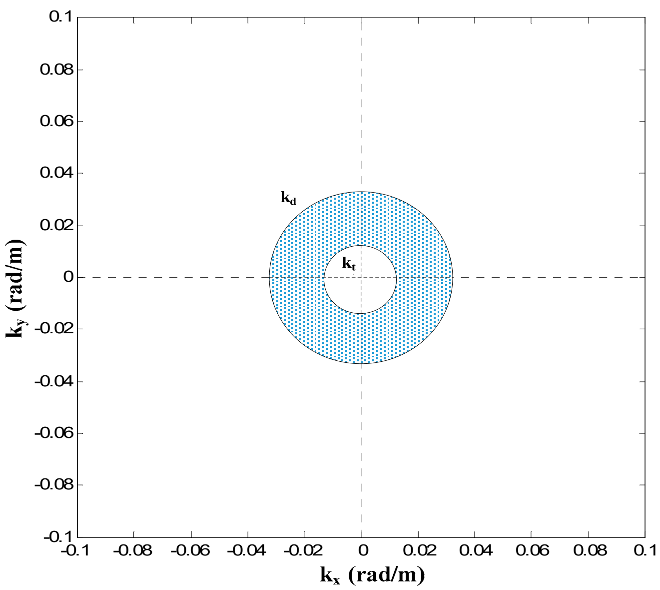

Figure 7. Small-scale wind streak energy spectrum.

As mentioned above, wind direction is retrieved based on the feature that small-scale streaks are assumed to be approximately parallel with the mean wind direction. We can find that the connection line of two energy concentrated areas is perpendicular to the wind streak, and then perpendicular to the wind direction. Figure 8 shows the filtered wind streak energy spectrum from the previously mentioned data set. The inner dotted circle represents the upper-limit, correspondingly, the outer circle represents the low-limit—both are labeled in this figure. The wind direction is perpendicular to the connection line of two energy concentrated areas. From this calculation, it is possible to obtain a vertical line of 36° and 144°, with respect to the north direction, and the 180° ambiguity problem was removed according to the quadrant comparison method. Therefore, this is an example of taking a radar image sequence and applying ESM to obtain the wind direction of 36°. It can be seen that the ESM result is far more agreeable with the anemometer data.

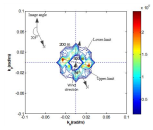

Figure 8. Wind direction retrieved from the filtered wind streak ES.

3.4. Complexity Analysis

The ARM is an improved variant of the traditional LGM. It utilizes the stability coefficient to judge the algorithm loop; recycles the adaptive reduction operator to reduce the image; and carries out two rounds of smoothing, before and after reduction. LGM employs a fixed number of judgments (three times); similarly, it applies a fixed two-order reduction operator to reduce the images, as well as applying the same smoothing process. The time complexity of the LGM is $5O(1)$(for the image processing) plus $O(n)$ (the gradient derivation), so the total algorithm complexity is $O(n)$. As a result of the increase in the calculation and cycle adaptive judgment, ARM takes longer than LGM; similarly, the time complexity is calculated as $kO(1)$ (k is random, with a maximum value of 8) plus $O(n)$, and as the ARM complexity equals LGM, both are $O(n)$.

The new ESM is used on the frequency domain characteristics to retrieve the wind direction. Compared with the other two methods, the computation time of ESM mainly lies in the two-dimensional discrete FFT transformation; however, there is no need to calculate the smoothing and shrinking process for each pixel in the image. At the same time, the small-scale wind band pass filter can be designed to completely separate the small-scale wind streak from the static feature image of the sea surface. Therefore, the information about the sea surface wind direction can be extracted more efficiently by using the feature of a small-scale wind streak parallel to the sea surface wind direction. However, time complexity of 2D FFT is $O(MN \log MN)$; in our algorithm, we made $M = N = 128$ (input image's resolution), so the entire time complexity comes down to $O(N^2 \log N)$.

Because the pixel gradients calculated by the two spatial algorithms (LGM and ARM) do not necessarily reflect the gradient directions of small-scale wind streaks, the inversion accuracy is not as good as the ESM algorithm. Nevertheless, ESM has a higher requirement for the size of the experimental area, and excessive measurement areas contain a lot of noise, which could increase the complexity of the wind streaks, while small measurement areas lead to incomplete wind streaks that will destroy the frequency domain characteristics of the wind steaks. In the application of ESM, experiments should be applied so as to select the appropriate research area, which increases the complexity of the algorithm. Additionally, the time complexity of EMS is a higher order than ARM and LGM, so this algorithm computation would be sensitive to the input image, meaning it will increase sharply with the growing input image resolution.

4. Testing and Results

4.1. Mathematical Metric for the Comparison

In order to measure the performance of the three inversion algorithms, this paper employs a metric of data error to analyze the errors between the inversion and reference wind direction. Let X_i be the time series of the inversion wind direction results, while Y_i refers to the reference wind direction time series, $i = 1, 2 \cdots N$ is the number of navigation radar image sequences used for the inversion of sea surface wind direction. We evaluated the performance of these algorithms by calculating the correlation coefficient, standard deviation, and bias between the inversion and reference wind direction. The calculation formula of these parameters are as follows:

$$A_i = Y_i - X_i \qquad \text{Error between the single retrieval and reference wind direction}$$

$$Bias = \overline{A} = \frac{1}{N}\sum_{i=1}^{N} A_i \qquad \text{Average deviation of two sequences}$$

$$Var = \frac{1}{N-1}\left(\sum_{i=1}^{N} A_i^2 - \frac{Bias^2}{N}\right) \qquad \text{Mean variance of two sequences}$$

$$\sigma = \sqrt{Var} = \sqrt{\frac{1}{N-1}\left(\sum_{i=1}^{N} A_i^2 - \frac{Bias^2}{N}\right)} \qquad \text{Standard deviation of two sequences}$$

$$r = \frac{\sum_{i=1}^{N}\left(X_i-\overline{X}\right)\left(Y_i-\overline{Y}\right)}{\sqrt{\sum_{i=1}^{N}\left(X_i-\overline{X}\right)^2\cdot\sum_{i=1}^{N}\left(Y_i-\overline{Y}\right)^2}} \qquad \text{Correlation coefficients of two sequences}$$

where $\overline{X} = \frac{1}{N}\sum_{i=1}^{N} X_i$ is the average value of the inversion wind direction, and $\overline{Y} = \frac{1}{N}\sum_{i=1}^{N} Y_i$ refers to the average wind direction. Compared with the other parameters, r is much more powerful for demonstrating the similarity between two sets of data, so in this paper, we choose r as the uniform perform evaluation metric, while $Bias$ and σ are simultaneously listed in following tables as the contrasts of the different algorithms.

The comparison of the operating times of the three algorithms is the average inversion time obtained by applying each algorithm to all of the data in the experiment. Because we focused on the post data processing, all of the data were tested using MATLAB software. Suppose t_i is one of the operating time series, then average operating time is as follows:

$$T = \frac{\sum_{i=1}^{N} t_i}{N} \tag{18}$$

4.2. Inversion Results

Figure 9 shows the comparison of the LGM and ARM wind direction from 180 sets of marine radar image-sequences with reference wind directions. Because the two algorithms are both operating in a space-domain, it would be feasible to put them together. The gray bars in the background are the wind speed measured by the anemometer Model-05103. We found wind speed ranges between 1.2–19.4 m/s. The results of ARM are more consistent with the reference wind direction, as shown in Figure 6, while the LGM curve shows a large jitter related to the reference wind direction, especially at a lower wind speed case, as shown from sampling points 29 to 64 in Figure 8.

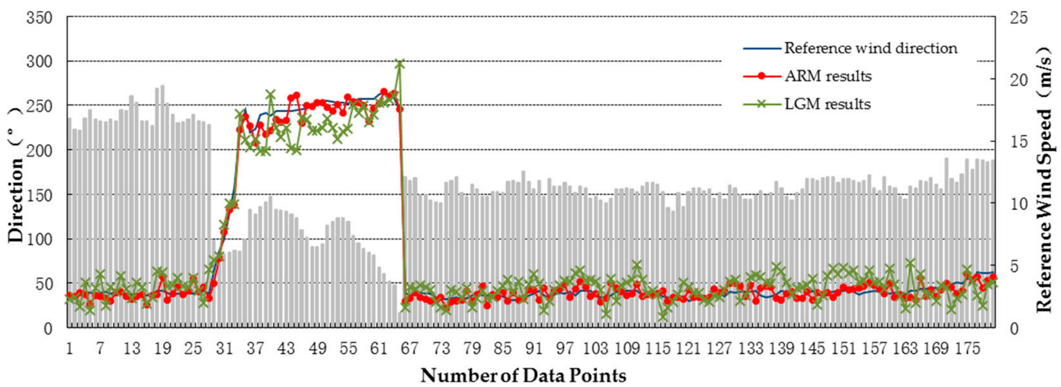

Figure 9. Results of the LGM and ARM algorithms compared with the reference wind directions.

It should be noticed that the discrepancy between LGM and the reference is larger than ARM. LGM's direction is always smaller than the reference in the numerical value, however, the results of LGM maintain a good consistency with the reference wind direction. Although there is a little jitter in the curve, it can quickly track the wind speed to get the ideal results. The comparison of LGM and ESM is in Figure 10.

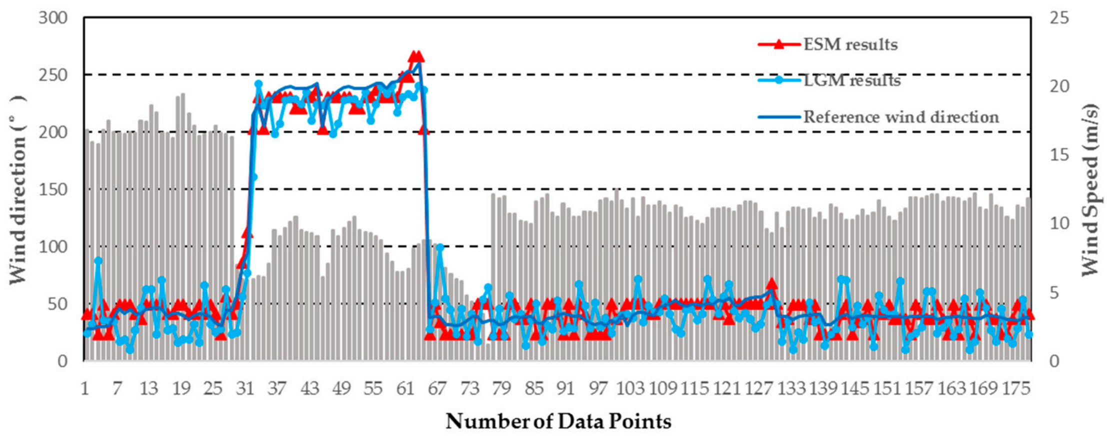

Figure 10. Results of the LGM and ESM algorithms compared with the reference wind directions.

It can be found that ESM contributes a similar performance to LGM, keeping an acceptable fluctuation trend as with LGM, and it can also track the reference values.

Table 2 shows the statistics of the error and running time between the retrieved and reference wind directions. From this information, in terms of the correlation coefficient, standard deviation, and deviation relative to the reference wind direction, we found that ARM is better than LGM and ESM. The correlation coefficient between ARM and the reference wind direction is 0.9956, which illustrates that it has a good consistency with the vane wind direction. The LGM coefficient is slightly inferior to ARM, while EMS establishes only 0.9523. At the same time, the mean differences and standard deviation of ARM are better than for LGM and ESM. the inversion accuracy of LGM and ESM are nearly the same. The last column of Table 2 shows that the average running times for processing a set of 32 radar images are 38.3, 27.1, and 20.5 s, respectively. EMS has the fastest operation time, nearly half that of ARM. From these results, we can conclude that ARM has a better retrieving accuracy compared with LGM and EMS, at the cost of a longer running time. EMS demonstrates a time efficient performance as a result of its spectrum character. LGM contributes a medium performance in the two aspects.

Table 2. Error and running time statistics between the retrieved and reference wind directions. ARM—adaptive reduced method; LGM—local gradient method; ESM—energy spectrum method.

Algorithm	Reference	Correlation Coefficient r	Standard Deviation σ (°)	Deviation *Bias* (°)	Average Running Time (s)
ARM results	Vane measured Wind direction	0.9956	7.62	−1.04	38.3
LGM results	Vane measured Wind direction	0.9832	17.33	1.18	27.1
ESM results	Vane measured Wind direction	0.9523	18.54	1.21	20.5

As ESM is sensitive to the measured area, for a deeper comparison of ARM and ESM, we picked 1494 sets of radar image sequences, and used both ARM and ESM to retrieve the wind direction, and to optimize an appropriate measurement area. Figure 11 shows the results of ARM and ESM compared with the reference wind directions. It can be found that both algorithms can provide satisfactory retrieving results in most cases, but a dramatic change exists with the reference wind directions between points 500 to 630, and the wind direction using even ARM cannot accurately reflect the wind direction fluctuation. In general, the ESM results are more identical to the reference, although there was always some jitter present in the green curve. By contrast, ARM maintained the up- and down-trend, especially when it comes upon an adverse wind direction, leading ineffective sampling points.

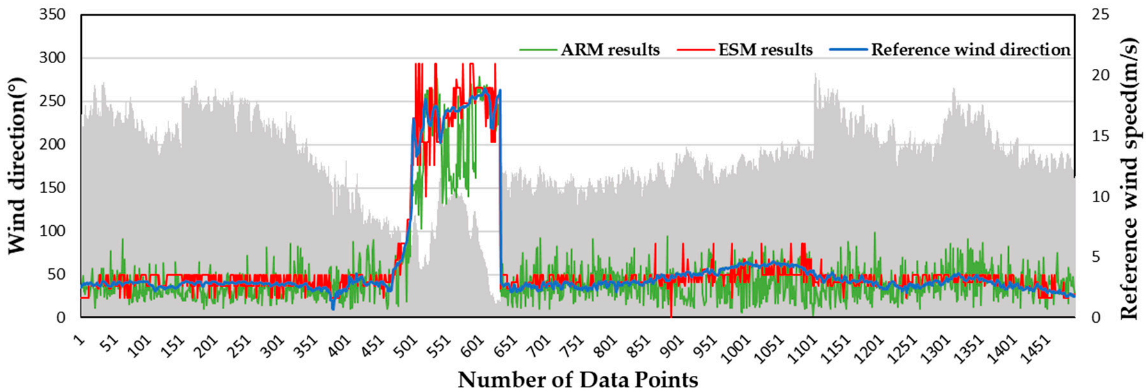

Figure 11. Results of the ARM and ESM algorithms compared with the reference wind directions.

Figure 12 shows the retrieving error distribution of the ARM (subplot-a) and ESM (subplot-b). Both of the retrieval algorithms have greater errors at a reference wind direction about 150°, because of the influence of typhoons and rain, but the ARM wind direction error is superior to that of ESM. The ESM wind direction errors range between −50° to 50°, whereas they are only −20° to 20° for the ARM errors. It can be inferred from the results that ESM is sensitive to rain-contaminated data, and the outlier points enlarge the retrieval range error for the data considered here.

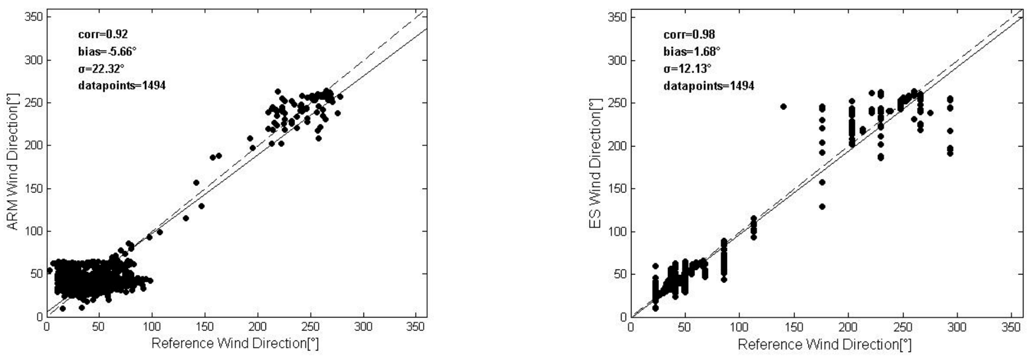

(**a**) (**b**)

Figure 12. The scatterplot of ARM and ESM: (**a**) the scatterplot of ARM; (**b**) the scatterplot of ESM.

The statistics of the wind direction results' error and average execution times for the 1494 datasets utilizing the ARM and ESM algorithms are shown in Table 3. It is shown that with an appropriate measured area, the results of ESM are superior to ARM in correlation, bias, and standard deviation, although it appears to have many more outlier points in rain-contaminated circumstance compared with ARM. The average running time of ESM is about 7 s less than that of ARM.

Table 3. Main statistical parameters and time of the ocean wind direction error.

Results	Correlation Coefficient r	Deviation *Bias* (°)	Standard Deviation σ (°)	Average Running Time (s)
ARM results	0.92	−5.66	22.32	25.2
ESM results	0.98	1.68	12.13	18.4

4.3. The Influence Factors

It can be found that ARM performs better than LGM in most aspects. Meanwhile, the preceding experimental results show that ARM and ESM are all in line with the engineering requirements for accuracy and running time. In the following, we will discuss the key factors than can influence algorithm performance, particularly for spatial-domain ARM and frequency-domain ESM, when using real-time data.

4.3.1. The Influence of the Measurement Area Size

For testing the influence of the measurement area size for ARM and ESM, we choose data with almost the same reference wind directions, wind speeds, and sea conditions, in order to make the experiment immune to other factors of interference. WE selected 227 sets of radar image sequences lasting 14 hours on 22 October 2010. In these data, the reference wind direction range was about 31°–43°, the reference wind speed range was about 13.3–19.6 m/s, the average wave height was 3.5 m, and the average wave direction equaled 93°.

The object region area had a radius ranging from 600 to 2100 m, and the azimuth direction ranged from 106°–69° anticlockwise. The measurement area was selected so as to be a square, with a side length lower bound at 500 m and upper bound at 2100 m, because the wind streak scale was 200–500 m. Finally, we took three typical measurement areas of 1485 m × 1485 m, 960 m × 960 m, and 720 m × 720 m, in order to apply the real measured area data to test the influence of the measurement area size.

The influence of the measurement area size on ARM and ESM is shown in Table 4. Here, ARM shows the highest precision in the measurement area, at 1485 m × 1485 m, because ARM retrieves the wind direction based on the small-scale wind streak spatial domain characteristics. The larger the measured area, the more wind streaks, that will lead to the measurement areas have the higher probability of the gradient direction. It demonstrates that if a large measurement area is available, the ARM would be more preferable. It shows that ESM has the highest precision in the measurement area of 960 m × 960 m from the table. Excessive measurement areas contain a lot of noise, which could increase the complexity of the wind streaks, while small measurement areas lead to incomplete wind streaks that will destroy the frequency domain characteristics of the wind steaks. Therefore, the ESM algorithm requires the measurement area to be validated and preprocessed in order to guarantee its performance. However, the average running time is less than that of ARM by about 6 s.

Table 4. Statistical parameters of wind direction considering different areas.

Measurement Area		1485 m × 1485 m	960 m × 960 m	720 m × 720 m
ARM results (°)	Deviation(°)	3.1	13.3	−20.7
	standard deviation (°)	13.2	15.1	27.7
	Correlation coefficient	0.99	0.95	−0.95
	Average running time (s)	24.4	24.3	23.7
ESM results (°)	Deviation (°)	−4.4	−2.2	−4.9
	Standard deviation (°)	9.03	5.6	9.6
	Correlation coefficient	0.99	0.99	0.99
	Average running time (s)	18.8	18.2	16.8

4.3.2. The Influence of Sea Surface Wind Speed

Next, we began to investigate the influence of the sea surface wind speed on retrieving the wind direction. By comparing the error of the wind direction results obtained from the 1494 sampling points, the results of ARM and ESM are shown in Figure 13a,b, respectively.

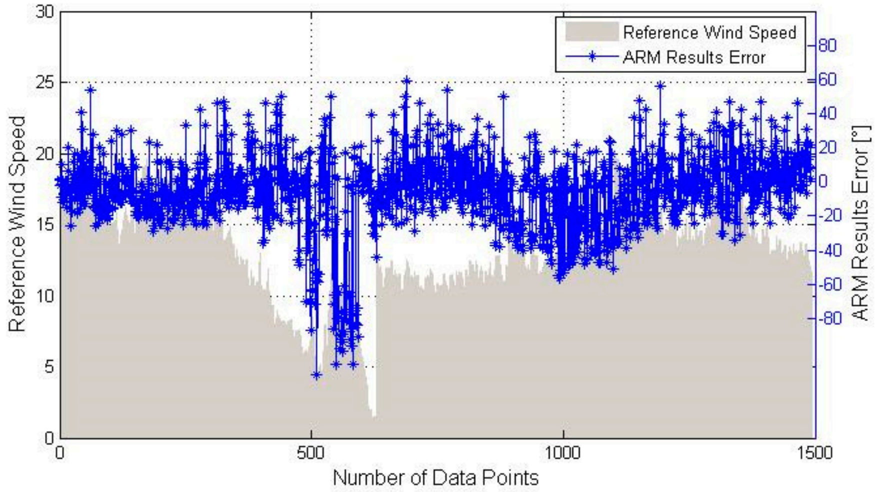

(**a**)

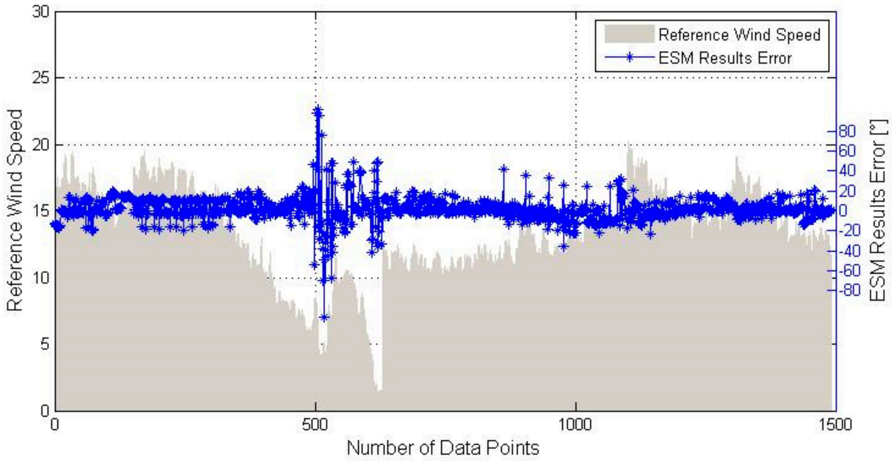

(**b**)

Figure 13. The influence of wind speeds on the error of ARM and ESM. (**a**) ARM; (**b**) ESM.

It can be found that both algorithms suffer large errors at about 500 sampling points, when the reference wind speed decreased sharply from 15 to 5 m/s. The errors became bigger because the small-scale wind streak was collapsed by the increasing ocean surface swell, due to the dramatic changes in wind speed. However, the ESM is much more robust against the uncertain interference. The main reason for this is that the ESM algorithm obtains the wind direction information from the wind streak energy spectrum. The energy spectrum band pass filter removes other streaks' features, which helps to eliminate the influence of the increased wind speed. The ARM algorithm obtains the wind direction information from the processing of small-scale wind streaks in the spatial domain, and the scale of the wind streak increases with the wind speed growth; hence, the characteristics of the reduced small-scale wind streak in the spatial domain will be lost as a result of the wind streak scale increasing, so ARM has a low accuracy in this case.

4.3.3. The Influence of Significant Wave Height

To test the influence of the wave height on ARM and ESM, we compared the wind direction under the data of the significant wave heights from 172 20-min long aligned sampling points of WAVEX. As shown in Figure 14, the average significant wave height in the data was in the range of 1–5 m. It can be found that the wind direction errors of both algorithms increased as the wave height increased.

When the significant wave height was less than 2 m, the wind direction error of the ARM was greater than ESM, but the acquisition point in this condition was too small to study. The wind direction error of ARM keeps on increasing when the significant wave height is more than 2 m, while the wind direction error of ESM is more stable in this case. The wind direction error of ESM has a slow growth, only when the significant wave height is more than 4.5 m.

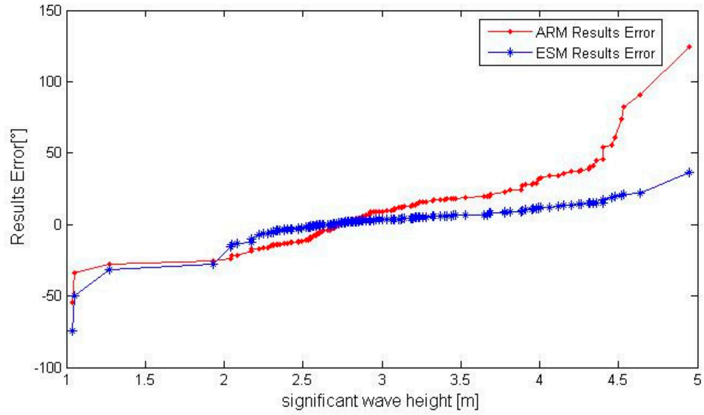

Figure 14. The influence of the significant wave height on the errors of ARM and ESM.

In general, the sea surface is almost swelling when the effective wave height is lower, and the wind field is relatively weak under this condition. The ESM algorithm seems to be more robust because swelling cannot break the small-scale wind streaks of the sea-surface wind field. In contrast, when the significant wave height is high, the sea surface is full of wind waves. It is easy to influence the ESM algorithm, because the small-scale wind streaks are not clear. However, for ARM, the characteristic image of the small-scale wind streak is obtained by the spatial domain reduction and filtering, once the significant wave height is high with increasing winds, it can be inferred that the wind direction error will increase, as the small-scale wind streak is collapsed.

4.3.4. The Influence of Near-Surface Current

To test the influence of the near-surface current on ARM and ESM, the near-surface current and reference wind direction from 172 20-min aligned acquisition points of WAVEX are shown in Figure 15, Figure 15a shows the relationship between the wind direction retrieving error and near-surface current, while Figure 15b gives the retrieving error and reference wind directions. In the following analysis, we considered the above-mentioned two factors at the same time. It should be noted that there were no data for the shored-based near-surface current at 110°–170°, as well as no data for the reference wind directions at 140°–200°.

It has been observed that the wind direction result errors have the most growth in the current at 180° to 200°, and in the reference wind direction at 0° to 50°, and the lower errors appear in the current at 60° to 120°, and in the reference wind direction at 200° to 240°. It is also shown that the error becomes the largest when the current direction is identical to the reference wind direction and is smallest in the opposite direction. For horizontally-polarized (HH-polarized) radars at grazing incidence, the NRCS has only one peak in the upwind direction, and has minimum in the crosswind direction. The influence of the sea-surface wind streaks' characteristics is relatively strong when the NRCS is a large value, further leading a severe wind retrieving error. From Figure 14, we find that the sea-surface current has almost no impact on the two wind direction algorithms. Both algorithms can retrieve a real-time wind direction, even in the varying near-surface current circumstances.

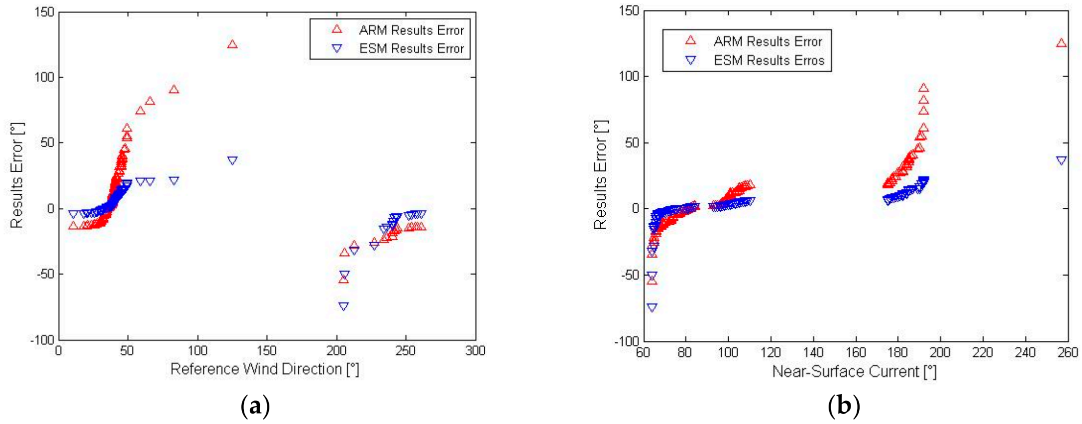

Figure 15. The influence of the near-surface current on the errors of ARM and ESM. (**a**) the relationship between the wind direction retrieving error and near-surface current; (**b**) the retrieving error and reference wind directions.

5. Conclusions

In this paper, we studied three celebrated wind direction retrieving methods—LGM, ARM, and ESM—based on small wind streaks extracted from X-band marine radar images. The data for the analyses were collected by the HEU wave monitoring system, and an anemometer on the Chinese South Coast, at Pingtan General Testing Ground. The contributions of this paper are that we give a straightforward comparison of the three methods, and their performances with real-world data are compared, with the additional analysis of the interference factors. The experiment results show that the ARM and ESM algorithms are better than LGM in terms of retrieving accuracy. However, LGM has the shortest running time, and it can be implemented for coarse-retrieving cases.

The ARM algorithm contributes a breakthrough, by retrieving the wind direction from the ocean surface in the spatial domain, and effectively suppresses the drawback of LGM. However, the ARM algorithm is computationally expensive, because it has more recursive cycles and an additional threshold judgment. Both LGM and ARM may overwhelm some characteristics of small-scale wind streaks, simultaneously losing part of the small-scale wind streak images. So, the performances of the spatial domain approaches cannot be guaranteed when the small-scale wind streaks' characteristics are not obvious. As ESM can automatically adapt to small-scale streak scale changes, it is robust with different data for retrieval, and with applying the band-bass filter. It can guarantee the quality of the separated small-scale wind streaks energy spectrum. Therefore, this method can provide an acceptable retrieving accuracy based on the data from X-band marine radars.

It has been shown that although ARM is inferior to ESM in terms of accuracy, it can cover most of the real-time requirements, and provide an acceptable performance. Furthermore, it requires only a single measurement area, compared with ESM. Taking the interference factors into account, ARM is susceptible to sea-surface wind speeds and significant wave heights, but is robust against sea-surface currents. ESM is almost robust against all of the interference factors, except for in a rain-contaminate environment; its wind direction results error increases only if the significant wave height is higher than 4.5 m. We draw a conclusion that ARM is better for real-time wind retrieving, while ESM is much more adaptable for post-data processing, with a superior retrieving performance. Future work will focus on the real-time implementation of the above-mentioned methods in real engineering areas with various circumstances.

Author Contributions: This paper is a collaborative work by all of the authors. H.W. proposed the idea, implemented the system, performed the experiments, analyzed the data, and wrote the manuscript. H.Q. and P.Z. helped to propose the idea, give suggestions, and revise the rough draft. L.W. helped to process the data from the raw sensors. W.C. helped for visualization work. R.A. and M.A.Z.R. helped to write the review and with editing, as well as doing some proofreading work.

Funding: The project was supported by the Natural Science Foundation of Jiangsu Province of China, under grant no. BK20180988; the National Natural Science Foundation of China (61801196); and the Natural Science Foundation of Higher Education Institutions of Jiangsu Province (17KJB510014).

Acknowledgments: We would like to thank the editor and reviewers for the efforts made in processing this submission, and we are particularly grateful to the reviewers for their constructive comments and suggestions, which helped us improve the quality of this paper.

Conflicts of Interest: The authors declare no conflict of interest.

References

1. Lund, B. Development and Evaluation of New Algorithms for the Retrieval of Wind and Internal Wave Parameters from Shipborne Marine Radar Data. Ph.D. Thesis, University of Miami, Miami, FL, USA, 2012.
2. Moat, B.I.; Yelland, M.J.; Molland, A.F. *The Effect of Ship Shape and Anemometer Location on Wind Speed Measurements Obtained from Ships*; University of Southampton: Southampton, UK, 2005.
3. Risien, C.M.; Chelton, D.B. A global climatology of surface wind and wind stress fields from eight years of QuikSCAT scatterometer data. *J. Phys. Oceanogr.* **2008**, *38*, 2379–2413. [CrossRef]
4. Lin, H.; Xu, Q.; Zheng, Q. An overview on SAR measurements of sea surface wind. *Prog. Nat. Sci.* **2008**, *18*, 913–919. [CrossRef]
5. Dankert, H.; Horstmann, J.; Rosenthal, W. Wind-and wave-field measurements using marine X-band radar-image sequences. *IEEE J. Ocean. Eng.* **2005**, *30*, 534–542. [CrossRef]
6. Hessner, K.; Borge, J.C.N.; Reichert, K. Estimation of the significant wave height with x-band nautical radars. In Proceedings of the 28th International Conference Offshore Mechanics and Arctic Engineering (OMAE), Madrid, Spain, 17–22 June 1999.
7. Wei, Y.; Zhang, J.-K.; Lu, Z. A novel successive cancellation method to retrieve sea wave components from spatio-temporal remote sensing image sequences. *Remote Sens.* **2016**, *8*, 607. [CrossRef]
8. Acobs, S.P.; O'Sullivan, J.A. Automatic target recognition using sequences of high resolution radar range-profiles. *IEEE Trans. Aerosp. Electron. Syst.* **2000**, *36*, 364–381. [CrossRef]
9. Wei, Y.; Lu, Z.; Yuan, G.; Fang, Z.; Huang, Y. Sparsity adaptive matching pursuit detection algorithm based on compressed sensing for radar signals. *Sensors* **2017**, *17*, 1120. [CrossRef] [PubMed]
10. Senet, C.M.; Seemann, J.; Ziemer, F. The near-surface current velocity determined from image sequences of the sea surface. *IEEE Trans. Geosci. Remote Sens.* **2001**, *39*, 492–505. [CrossRef]
11. Dankert, H. Retrieval of surface-current fields and bathymetries using radar-image sequences. In Proceedings of the Geoscience and Remote Sensing Symposium (IGARSS'03), Toulouse, France, 21–25 July 2003; pp. 2671–2673.
12. Gommenginger, C.P.; Ward, N.P.; Fisher, G.J.; Robinson, I.S.; Boxall, S.R. Quantitative microwave backscatter measurements from the ocean surface using digital marine radar images. *J. Atmos. Ocean. Technol.* **2000**, *17*, 665–678. [CrossRef]
13. Lee, P.H.Y.; Barter, J.D.; Beach, K.L.; Hindman, C.L.; Lake, B.M.; Rungaldier, H.; Shelton, J.C.; Williams, A.B.; Yee, R.; Yuen, H.C. X band microwave backscattering from ocean waves. *J. Geophys. Res. Ocean.* **1995**, *100*, 2591–2611. [CrossRef]
14. Hatten, H.; Seemann, J.; Horstmann, J.; Ziemer, F. Azimuthal dependence of the radar cross section and the spectral background noise of a nautical radar at grazing incidence. In Proceedings of the International Geoscience and Remote Sensing Symposium, Seattle, WA, USA, 6–10 July 1998; pp. 2490–2492.
15. Huang, W.; Liu, X.; Gill, E. Ocean wind and wave measurements using X-band marine radar: A comprehensive review. *Remote Sens.* **2017**, *9*, 1261. [CrossRef]
16. Lu, Z.; Yang, J.; Huang, Y. Sea wind direction extraction algorithm by X-band radar in moving platform. *Syst. Eng. Electron.* **2016**, *38*, 799–803.
17. Lund, B.; Graber, H.C.; Romeiser, R. Wind retrieval from shipborne nautical X-band radar data. *IEEE Trans. Geosci. Remote Sens.* **2012**, *50*, 3800–3811. [CrossRef]
18. Vicen-Bueno, R.; Horstmann, J.; Terril, E.; De Paolo, T.; Dannenberg, J. Real-time ocean wind vector retrieval from marine radar image sequences acquired at grazing angle. *J. Atmos. Ocean. Technol.* **2013**, *30*, 127–139. [CrossRef]

19. Liu, Y.; Huang, W.; Gill, E.W.; Peters, D.K.; Vicen-Bueno, R. Comparison of algorithms for wind parameters extraction from shipborne X-band marine radar images. *IEEE J. Sel. Top. Appl. Earth Observ. Remote Sens.* **2015**, *8*, 896–906. [CrossRef]
20. Forget, P.; Saillard, M.; Guérin, C.A.; Testud, J.; Le Bouar, E. On the use of x-band weather radar for wind field retrieval in coastal zone. *J. Atmos. Ocean. Technol.* **2016**, *33*, 899–917. [CrossRef]
21. Dankert, H.; Horstmann, J.; Koch, W. Ocean wind fields retrieved radar image sequences. In Proceedings of the IEEE International Geoscience Remote Sensing Symposium, Toronto, ON, Canada, 24–28 June 2002; pp. 2150–2152.
22. Dankert, H.; Horstmann, J. A marine radar wind sensor. In Proceedings of the International Geosciences and Remote Sensing Symposium, Denver, CO, USA, 31 July–4 August 2006; pp. 1296–1299.
23. Dankert, H.; Horstmann, J. Wind measurements at FINO-I marine radar image sequences. In Proceedings of the IEEE International Geoscience Remote Sensing Symposium, Seoul, Korea, 25–29 July 2005; pp. 1777–1780.
24. Dankert, H. A marine radar wind sensor. *J. Atmos. Ocean. Technol.* **2007**, *24*, 1629–1642. [CrossRef]
25. Wang, H.; Lu, L. Determination of X-band radar images ocean wind direction using ARM. *J. Huazhong Univ. Sci. Technol. (Nat. Sci. Ed.)* **2015**, *10*, 42–47.
26. Wang, H.; Lu, Z. Wind direction retrieved based on energy spectrum from X-band radar image sequences. *J. Comput. Theor. Nanosci.* **2016**, *13*, 8288–8297. [CrossRef]
27. Dankert, H.; Horstmann, J.; Rosenthal, W. Ocean surface winds retrieved from marine radar image sequences. In Proceedings of the International Geosciences and Remote Sensing Symposium, Anchorage, AL, USA, 20–24 September 2004; pp. 1903–1906.
28. Lu, Z.; Yang, Y.; Huang, Y. Research on the improvement on the algorithm for retrieving wave height from shadow in the marine radar images. *Chi. J. Sci. Instr.* **2017**, *38*, 212–218.
29. Lu, Z.; Yang, Y.; Huang, Y. Research on correlation in spatial domain to eliminate the co-channel interference of the X-band marine radar. *Syst. Eng. Electron.* **2017**, *39*, 758–767.
30. Etling, D.; Brown, R.A. Roll vortices in the planetary boundary layer: A review. *Bound. Layer Meteorol.* **1993**, *65*, 215–248. [CrossRef]
31. Brow, R. A secondary flow model for the planetary boundary layer. *Atoms. Sci.* **1970**, *27*, 742–757. [CrossRef]
32. Gerling, T.W. Structure of the surface wind field from the Seasat SAR. *J. Geophys. Res. Ocean.* **1986**, *91*, 2308–2320. [CrossRef]
33. Wang, H.; Lu, Z. Research on small scale wind streak factor of marine radar-image sequences. In Proceedings of the 8th International Symposium on Computational Intelligence and Design (ISCID), Hangzhou, China, 12–13 December 2015; pp. 335–339.